Weierstraß-Institut
für Angewandte Analysis und Stochastik

im Forschungsverbund Berlin e.V.

Preprint ISSN 0946 – 8633

Marangoni-driven liquid films rising out of a meniscus onto a nearly horizontal substrate

Andreas Münch[1] and P. L. Evans[2]

submitted: 11. Juni 2004

[1] Email: muench@mathematik.hu-berlin.de

[2] Email: pevans@mathematik.hu-berlin.de

[1,2] Address for correspondence: Humboldt University of Berlin
Institute of Mathematics
10099 Berlin, Germany

No. 941

Berlin 2004

2000 *Mathematics Subject Classification.* 76D08, 37N10, 34B60, 34E10, 76D27, 76D45, 76B45, 76A20 .

Key words and phrases. Lubrication theory, Gravity and surface tension driven liquid flows, undercompressive waves, Landau-Levich drag-out problem, coating flows.

Work supported by DFG grant MU 1626/3-1 and by the DFG Research Center FZT 86.

Edited by
Weierstraß-Institut für Angewandte Analysis und Stochastik (WIAS)
Mohrenstraße 39
10117 Berlin
Germany

Fax: + 49 30 2044975
E-Mail: preprint@wias-berlin.de
World Wide Web: http://www.wias-berlin.de/

Abstract

We revisit here the situation of a thin liquid film driven up an inclined substrate by a thermally induced Marangoni shear stress against the counter-acting parallel component of gravity. In contrast to previous studies, we focus here on the meniscus region, in the case where the substrate is nearly horizontal, so there is a significant contribution from the normal component of gravity. Our numerical simulations show that the time-dependent lubrication model for the film profile can reach a steady state in the meniscus region that is unlike the monotonic solutions found in [Münch, SIAM J. Appl. Math., 62(6):2045-2063, 2002]. A systematic investigation of the steady states of the lubrication model is carried out by studying the phase space of the corresponding third order ODE system. We find a rich structure of the phase space including multiple non-monotonic solutions with the same far-field film thickness.

1 Introduction

In recent years, various aspects of the formation and behavior of thin liquid films that climb out of a reservoir along an inclined wafer under the action of a thermally induced Marangoni shear stress have been intensively investigated, e. g. [1, 3, 4, 5, 8, 9]. The basic setup, introduced in the first reference, is shown in Fig. 1. A silicon wafer, tilted at an angle α from the vertical position, is subject to a temperature gradient between two heaters that maintain a temperature of T_+ at its lower end, and of $T_- < T_+$ at its upper end. The lower end of the wafer is submerged in a reservoir of silicon oil. At the beginning of the experiment, the level of the liquid in the reservoir is kept below the region where the temperature gradient sets in. The fluid therefore achieves a thermal and hydrostatic equilibrium, with a meniscus that extends a certain distance up the wafer.

Then, the liquid of the reservoir is raised, by slowly adding liquid from an external supply (not shown in the figure), until the meniscus just reaches into the thermal gradient region. As a result, the liquid in the upper part of the meniscus experiences a thermal gradient, which leads to a gradient in the temperature dependent surface tension coefficient, so that the surface tension increases with distance above the reservoir. Consequently, a Marangoni shear stress sets in at

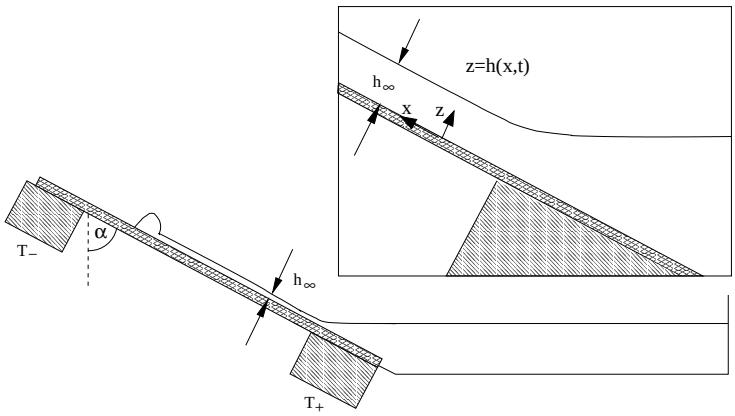

Figure 1: Sketch of the experimental setup with the wafer in a close to horizontal position (i. e. at a large inclination angle α with respect to the vertical position). The substrate is subject to a temperature gradient between the heaters that are held at temperatures $T_+ > T_-$. This induces a Marangoni shear stress that moves a thin liquid film up the wafer.

the liquid/air interface, which pulls a thin film of liquid out of the reservoir, up along the wafer.

Once the contact line has moved sufficiently far from the reservoir's surface, the film profile becomes stationary near the meniscus. For some distance above the meniscus, the film has a nearly uniform thickness h_∞. Towards the rising contact line, the film can evolve into either a single traveling wave or a double wave structure [1, 2]. In the latter case, the leading part of the double wave is a nonclassical undercompressive wave. Further work extended these results on the wave dynamics in a number of directions [13, 17]. It has been found that the film thickness h_∞ plays an important role in determining the outcome, i.e., which of the different wave structures evolve. Various aspects of the film profiles in the contact line region, including their stability, have also been studied in [8, 9].

The film thickness h_∞ has usually been treated as an independent parameter in the aforementioned theoretical investigations, but for the experimental setup discussed here and in most of the above references, h_∞ is typically determined by the meniscus. This phenomenon is related to the Landau-Levich drag-out problem of determining the thickness of an isothermal liquid film deposited onto a substrate that is pulled out of a liquid reservoir. Using ideas from matched asymptotics, Landau and Levich [11] were able to understand how the meniscus that forms where the substrate leaves the reservoir controls the thickness h_∞. They provided a leading order result for the thickness as a function of the liquid properties and the withdrawal speed, for the case of a vertical substrate.

Landau and Levich's ideas were extended to the Marangoni-driven film and non-zero inclination angles by Cazabat et al. [3]. A subsequent study [5] revealed

a systematic deviation of theory and experimental thickness measurements of up to about 20%. This discrepancy is connected to the presence of logarithmic terms in the next order corrections [15, 21]. Münch [15] provides a derivation of the complete correction term for non-zero inclination angles via a systematic application of matched asymptotics. These results, however, did not extend to the regime of moderate and large inclination angles, i.e., substrates that are tilted close to a horizontal position.

In this paper, we focus on the situation of nearly horizontal wafers, that is, inclination angles α that satisfy $\cot\alpha \ll 1$, by first performing numerical simulations of the time dependent lubrication model for the two-dimensional flow, and then investigating the phase space of the third order ODE that describes a stationary meniscus. Our study reveals a number of new meniscus solutions which typically persist if we perturb the value of h_∞, i.e., these solutions do not select the thickness h_∞ ahead of the meniscus.

These findings are related to similar results for coating films on a stationary or moving substrate obtained by a number of authors following Landau and Levich's work. Wilson [22] investigated the drag-out problem for general inclination angles, and determined the film thickness by solving, via matched asymptotics, a boundary value problem for the free surface. He noticed a non-uniformity in his solution as α approached $\pi/2$, and observed that the the meniscus solution ceased to exist if $\pi/2 - \alpha$ was smaller than a critical value (depending on the withdrawal speed). Furthermore, Wilson observed that these solutions were not always unique. The latter issue was taken up again by Hocking [7], who recognized the importance of the contact-line region in determining the film thickness for a range of withdrawal speeds. Kheshgi et. al. [10] also discussed the steady state problem for the meniscus region and identified two types of solutions, one that fixes the flow rate according to the wall velocity and reservoir configuration, and a second type where the flow rate can be chosen independently. However, none of these authors systematically investigated the three-dimensional phase space of the steady state ODEs.

The paper is organized as follows: In Section 2, we formulate the dimensional model for the meniscus/film driven by Marangoni shear stresses and give scalings that lead to a lubrication model that is valid in the entire film including the meniscus. Section 3 presents results of numerical simulations showing different examples of how a meniscus can evolve starting from monotonic initial data. Stationary solutions satisfying the meniscus far-field conditions are considered in Section 4 via investigation of the three-dimensional phase space of the corresponding third order ODE. In Section 5, we summarize and discuss our results.

2 Formulation

In [15], a stationary model was derived for the meniscus profile using ideas from singular perturbation theory to reduce the free boundary problem for the coupled Stokes and energy equations to a boundary value problem for a scalar third order ODE for the case $\alpha > 0$. The corresponding boundary value problem for a vertical wafer position was given in [21] and the time-dependent fourth order PDE was used in [16] to investigate the pinch-off instability in an experiment by Ludviksson and Lightfoot [12]. Generalizing these approaches, the evolution of the dimensionless film/meniscus profile $z = h(x,t)$ is governed by

$$h_t + \Omega\,(h^2)_x - (h^3)_x = -\left(h^3\kappa_x\right)_x + D\left(h^3 h_x\right)_x, \tag{1}$$

where

$$\kappa = \frac{h_{xx}}{(1+\epsilon^2 h_x^2)^{3/2}}$$

is the nonlinear expression for curvature. The quadratic and cubic terms on the left side of (1) represent the contribution of the Marangoni shear stress (where the prefactor Ω, represents a temperature profile, explained further below) and the counteracting component of gravity parallel to the wafer. On the right hand side, the first term arises from surface tension and the second from the contribution of the normal component of gravity.

The above equation was non-dimensionalized using the following scalings for x, z and t, respectively,

$$L = \left(\frac{3\sigma\gamma\sigma_T}{2\rho^2 g^2\cos^2\alpha}\right)^{1/3}, \quad H = \frac{3\gamma\sigma_T}{2\rho g\cos\alpha}, \quad \tau = \frac{2^{5/3}\mu\,(\sigma\rho g\cos\alpha)^{1/3}}{3^{2/3}(\gamma\sigma_T)^{5/3}}, \tag{2}$$

and contains two dimensionless parameters, the length scale ratio ϵ and the parameter D, which measures the relative importance of the normal component of gravity. These are defined by

$$\epsilon := \frac{H}{L} = \left(\frac{9}{4}\frac{\gamma^2\sigma_T^2}{\sigma\rho g\cos\alpha}\right)^{1/3} \qquad \text{and} \quad D := \frac{\epsilon}{\cot\alpha}. \tag{3}$$

The dimensional quantities that appear here are the mean surface tension of the liquid/air interface σ, the temperature gradient γ, the dependence of surface tension on temperature $\sigma_T = d\sigma/dT$, the liquid viscosity μ, the density ρ, and the gravitational acceleration g.

Previous work by Münch [15] introduced a temperature profile $\Omega = \Omega(x)$ that cuts off surface tension gradients in the meniscus region near the lower heater. The rationale for this choice is the actual experimental setting where the temperature gradient, hence the surface tension gradient, is constant along the substrate and

the film except near the heaters, where it drops to zero. The cut-off was set at a fixed distance along the x-axis below the rising height for an isothermal, static meniscus on a perfectly wetting substrate. Preliminary numerical studies indicate that this distance must be increased for nearly horizontal wafer inclinations to maintain the liquid flow up the substrate [14]. This can be achieved, for example, by specifying the cut-off in terms of h, so that $\Omega = \Omega(h)$ is set to zero once h exceeds a threshold of about $l_{\rm cap}/H$, and to one elsewhere. This means that in physical units, the cut-off is imposed where the liquid layer is about one capillary length $l_{\rm cap} = (\sigma/(\rho g))^{1/2} \approx 1$ mm deep and therefore does not interfere with the wave structures that evolve in the sub-millimetric film in front of the meniscus. In the scalings (2), the cut-off thickness turns out to be $l_{\rm cap}/H = 1/(\epsilon D^{1/2})$, which tends to infinity for $\epsilon \to 0$ and $D \ll \epsilon^{-2}$. This permits us to set Ω to one, as long as we focus on the leading order behavior of (1) with respect to this limit.

Eqn. (1) requires boundary conditions. Far above the meniscus, we use a precursor model to alleviate the well-known singularity near a moving contact line,

$$h(x,t) \to b \qquad \text{for} \quad x \to \infty. \tag{4}$$

In the other direction, the meniscus flattens out onto the surface of the undisturbed reservoir,

$$h(x,t) \sim -x/D \qquad \text{for} \quad x \to -\infty. \tag{5}$$

In typical physical experiments [3, 4, 19, 20], the capillary number $3\mu(L/\tau)/\sigma$ is small, characterizing flows where surface tension dominates viscous stresses. It turns out that the length scale ratio $\epsilon = H/L$ is the cubic root of the capillary number and is therefore small itself, so that we can expect lubrication theory to be valid as long as film slopes h_x remain reasonable. Critically large values for h_x can arise in particular in the meniscus region near the reservoir for vertical or nearly vertical positions of the substrate, which is why the nonlinear expression for curvature was retained in (1), cf. [15]. On the other hand we restrict ourselves in this paper to nearly horizontal wafer positions, so $\alpha \sim \pi/2$, i.e., $\cot\alpha \ll 1$. Using (3) and (5), we get $\epsilon|h_x| = \epsilon/D \ll 1$ in the meniscus region near the reservoir. Then κ reduces, to leading order, to the linearized curvature expression h_{xx}.

Hence, we obtain the following lubrication model for $h(x,t)$

$$h_t + [f(h)]_x = -\left(h^3 h_{xxx}\right)_x + D\left(h^3 h_x\right)_x, \tag{6}$$

where $f(h) := h^2 - h^3$ denotes the *flux-function*, as a valid approximation to (1) if $\epsilon \ll D \ll \epsilon^{-2}$. In the following section, we discuss (6) with far-field conditions (4) and (5) for $D > 0$.

3 Dynamical Simulation

We seek solutions for the PDE (6) using initial data which satisfies the far-field conditions (4) and (5). Specifically, the initial profile for our computations consists of a static meniscus smoothly joined to the precursor film. The static meniscus arises in the absence of Marangoni forces through the balance of mean surface tension and gravity. Its profile is governed by the ODE $h_{xxx} = Dh_x + 1$ and the boundary conditions $h \sim -x/D$ for $x \to -\infty$ and $h(0) = 0 = h_x(0)$. The conditions at $x = 0$ ensure that the 'tip' of the meniscus is located at the origin and levels out onto the substrate with zero contact angle. Raising this profile by an amount b permits it to be smoothly joined to a precursor film starting at $x = 0$. Thus, the initial profile is:

$$h_0(x) = \begin{cases} D^{-3/2}\left(\exp(D^{1/2}x) - D^{1/2}x - 1\right) + b & \text{for} \quad x \le 0, \\ b & \text{for} \quad x > 0. \end{cases} \tag{7}$$

To obtain solutions of (6) numerically, we truncate the infinite spatial domain to $[x_1, x_2] = [-l/5,\ 4l/5]$, with the length of the domain chosen to be about $l = 100$. We impose four boundary conditions, requiring $h_x(x_2, t) = 0$, $h_{xxx}(x_2, t) = 0$ and $h(x_1, t) = h_0(x_1)$, $h_{xxx}(x_1, t) = 0$ for $t > 0$. We discretize the initial boundary value problem on this domain using standard finite differences in space and an implicit Euler scheme in time. Grid points are concentrated near where the evolving wave structure joins the precursor. After each time step, the solution is transferred via interpolation onto a new grid shifted to match the new position of the leading front. The time discretization error is controlled using a step-doubling approach. All calculations are carried out in quadruple precision arithmetic in order to obtain accurate results for fourth order PDEs discretized on a fine grid [18].

In the following, we consider three examples, using a fixed value of $b = 0.005$ for the precursor film thickness with three different values for $D = 0.1021$, 0.3220, and 0.6426. For a fixed temperature gradient, increasing the parameter D corresponds to lowering the wafer to more horizontal positions in a physical experiment.

Example 1: $D = 0.1021$.

At first, a rapidly growing ridge forms at the meniscus. The ridge then separates off and begins to rise up the wafer. For the smallest choice of D, the shape of the ridge saturates, forming a single compressive wave, traveling with constant speed in the positive x direction (see Figure 2(a)). As explained for example in [2], the term compressive (or Lax) wave refers to the fact that the characteristic speeds for the left and right state h_∞ and b satisfy the so-called Lax entropy condition $f'(h_\infty) < s(h_\infty, b) < f'(b)$, where the wave speed s is given by the

Rankine-Hugoniot condition $s = (f(h_\infty) - f(b))/(h_\infty - b)$. As it moves further away, the meniscus settles into a monotonic, stationary solution with h_∞ as far-field thickness for large positive x. The value of h_∞ depends on D but is not affected if we perturb the value of b.

Example 2: $D = 0.3220$.

For this somewhat larger value of D, the shape of the capillary ridge does not saturate, in contrast to the previous example. We see in Fig. 2(b) that a ridge forms as before, but begins to pull apart to form the typical profile of a double wave with two separating fronts. The leading wave is a nonclassical undercompressive wave with a unique, b and D-dependent left state $h_{\rm uc}$ for which the Lax condition is violated (i.e. $f'(h_{\rm uc}) < s(h_{\rm uc}, b)$), while the trailing wave is a classical compressive or Lax wave; a detailed investigation of the double wave can be found in [1, 2, 13]. The compressive wave moves at a lower speed than the undercompressive wave, but both speeds are positive, so that for long times, the meniscus evolves into a stationary monotonic solution with far-field film thickness h_∞ which depends on D but not on b, as in the first example.

Example 3: $D = 0.6426$.

For the largest value of D we consider in this section, the development in the beginning is similar to the second example: We see the formation of an undercompressive wave (Fig. 3), that moves up the wafer. In its wake, a structure with a visible dip emerges, which, however, remains attached to the meniscus, i.e. it persists even for long times as the undercompressive wave moves further up the wafer. Therefore, the meniscus evolves into a stationary profile that is non-monotonic, with $h_\infty = h_{\rm uc}$. Thus in this example, the far-field thickness is set by the undercompressive wave, so it depends on b in addition to D.

We note that in a physical experiment, the oscillatory structure that evolves in the meniscus profile closely resembles a Lax wave moving at zero speed. Interestingly, such a structure was reported by Schneemilch and Cazabat [19] for a large inclination angle of $\alpha = 70°$.

4 Steady state solutions

4.1 Steady state equations

We next explicitly seek steady state solutions of equation (6). Setting $h_t = 0$ and integrating once yields a third-order ODE for h,

$$h_{xxx} - Dh_x = -\frac{f(h) - Q}{h^3}, \tag{8}$$

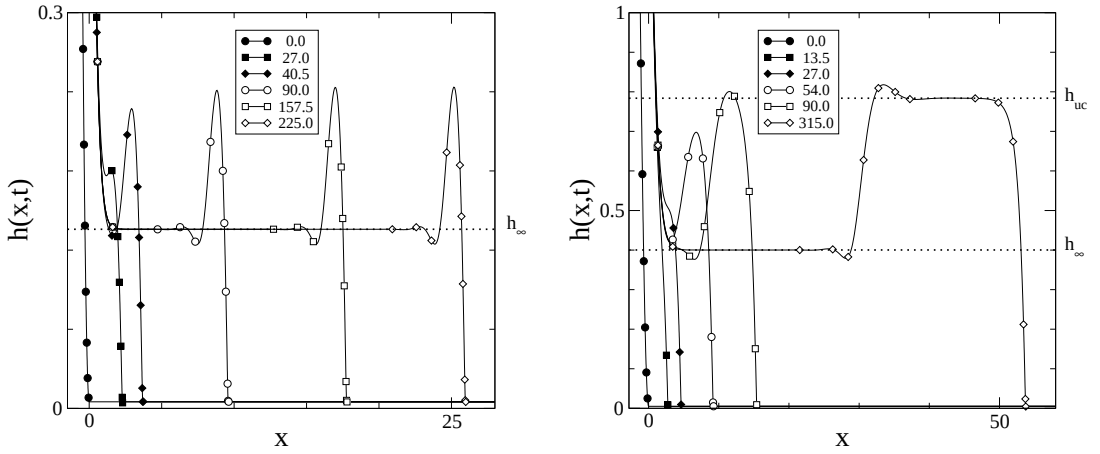

Figure 2: Numerical solutions of (6), (7) for example 1 (Fig. 2(a), left) and example 2 (Fig. 2(b), right). Film profiles are shown at dimensionless times as given in the legends. Note there is a thin precursor film of thickness $b = 0.005$ in both cases.

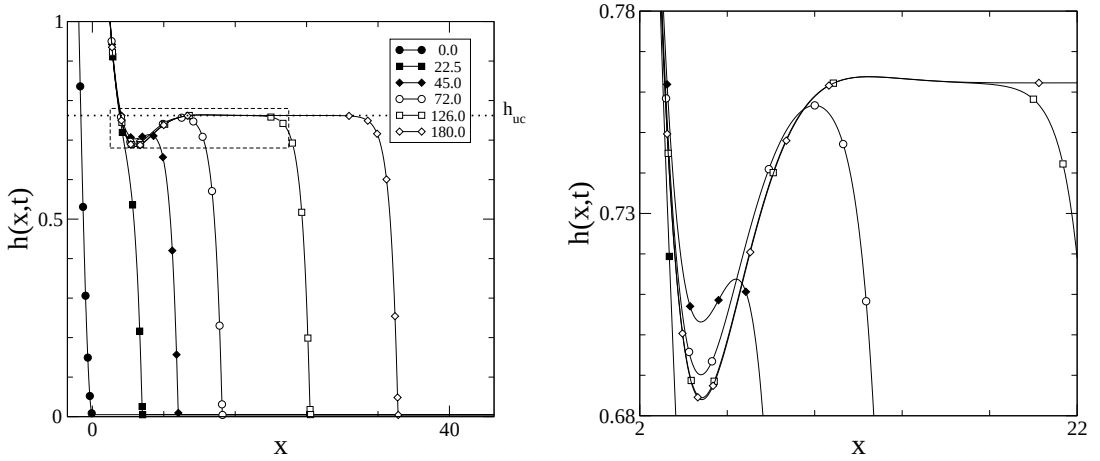

Figure 3: Numerical solution of (6), (7) for example 3, at dimensionless times given in the legends. The right figure (Fig. 3(b)) shows an enlarged view of the region in the left figure (Fig. 2(a), left) delineated by a dashed box. Again the precursor layer thickness is $b = 0.005$.

where the constant of integration Q represents the total flux of liquid across a cross-section of the film. Specifically we look for solutions that extend from the reservoir at $x \to -\infty$ onto a flat film at $x \to \infty$, i.e. that satisfy the far-field conditions

$$h(x,t) \sim h_\infty \qquad \text{for} \quad x \to \infty, \tag{9}$$

$$h(x,t) \sim -x/D \qquad \text{for} \quad x \to -\infty. \tag{10}$$

From (8) and (9), we readily find that Q and h_∞ are related via the flux function, $Q = f(h_\infty)$. For given Q in the range $0 \leq Q < f(2/3) = 4/27$, there are exactly two solutions h_∞ that satisfy this relation. The lower solution, h_B, lies in the range $0 < h_B < 2/3$ and increases with Q, while the upper, h_T, satisfies $2/3 < h_T < 1$ and decreases. For $Q \to 0$, h_B and h_T tend to 0 and 1, respectively, and for $Q \to 4/27$, they merge at $h = 2/3$.

In the following, we identify the solutions of (8)-(10) with h_∞ equal to either h_B or h_T, by investigating the three-dimensional phase space of (8). There are two parameters in (8), D and Q. However, rather than using Q itself as second parameter, we use the corresponding lower film thickness h_B, $0 < h_B < 2/3$. From h_B we can determine the total flux $Q = f(h_B)$, and the upper thickness h_T, $2/3 < h_T < 1$, by solving $f(h_T) = Q$. As is made clear below, the solutions of (8)-(10) with far-field thickness $h_\infty = h_B$ are qualitatively distinct from those where $h_\infty = h_T$. We will subsequently refer to the former as Type I and to the latter as Type II meniscus solutions.

Letting $v = h'$ and $w = h''$, we convert (8) into a system of three first order ODEs

$$h' = v, \qquad v' = w, \qquad w' = Dv - \frac{f(h) - f(h_B)}{h^3}, \tag{11}$$

where primes denote derivatives with respect to x.

4.2 Equilibria and invariant manifolds

The system (11) has two equilibria, the 'bottom' equilibrium $B = (h_B, 0, 0)$ and the 'top' equilibrium $T = (h_T, 0, 0)$. Linearizing (11) near an equilibrium $I \in \{B, T\}$, we find the characteristic equation for the eigenvalues of the linearized ODE system to be

$$\lambda^3 - D\lambda + f'(h_I)/h_I^3 = 0. \tag{12}$$

For both choices of $I \in \{B, T\}$, the roots of this polynomial equation have non-zero real part since $f'(h_I)$ is non-zero. Moreover, the sum of the three roots of (12) must be zero, so there must be real roots or real parts of complex conjugate roots of both signs, hence B and T are saddle points.

For the bottom fixed point, we have $f'(h_B) > 0$, so that the product of the eigenvalues must be negative. This implies that exactly one eigenvalue is real and

negative, the other two are either real and positive or form a complex conjugate pair with positive real part. The distinction between these two cases is provided by the sign of the discriminant

$$\Delta(h; D) = -\frac{D^3}{27} + \frac{(f'(h)/h^3)^2}{4}. \tag{13}$$

If $\Delta(h_B; D) > 0$, we have a complex conjugate pair, for $\Delta(h_B; D) \leq 0$, all roots are real. Hence B has a one-dimensional stable manifold $W^s(B)$ and a two-dimensional unstable one, $W^u(B)$. Trajectories on the latter form a spiral near B in the case where we have a complex conjugate pair of eigenvalues, i.e., if $\Delta(h_B; D)$ is positive.

For the top fixed point, $f'(h_T) < 0$, so it has a one-dimensional unstable manifold $W^u(T)$ and a two-dimensional stable manifold $W^s(T)$. The eigenvalue corresponding to $W^u(T)$ is real while the eigenvalues for $W^s(T)$ are complex conjugate exactly if $\Delta(h_T; D) > 0$; in that case, the trajectories on $W^s(T)$ wind into a spiral near T. For $\Delta(h_T; D) \leq 0$, all eigenvalues are real.

We now turn to characterizing the trajectories that have the proper behavior for $x \to -\infty$, i.e. that satisfy (10). Expanding h in terms of x yields a special solution, $h_0(x)$, the first terms of which are

$$h_0(x) = -\frac{x}{D} - \ln|x| + o(1) \qquad \text{at} \quad x \to -\infty. \tag{14}$$

The behavior of the general solution of (8) at $x \to -\infty$ that satisfies (10) is given by

$$h(x) \sim h_0(x) + C_0 + C_1 \exp\left(D^{1/2}x\right) \qquad \text{at} \quad x \to -\infty. \tag{15}$$

Here, C_0 and C_1 are arbitrary constants. The first of these two constants, C_0, corresponds to translations of the solution along the x-axis; since solutions to (8)-(10) are translation invariant, we can set $C_0 = 0$ without loss of generality. From this, we conclude that the solutions of (8) that satisfy (10) form a one parameter family, which corresponds to a two-dimensional manifold W^∞ in the phase space for (11). We note that solutions satisfying the far field condition (10) can be represented as trajectories approaching an equilibrium, by writing (8) as a new system of ODEs with independent variables $\tilde{u} = 1/h$, $\tilde{v} = h_x$ and $\tilde{w} = h_{xx}$. Then these solutions become trajectories of the new system that tend to the equilibrium $(\tilde{u}, \tilde{v}, \tilde{w}) = (0, -1/D, 0)$. In this paper, however, we continue with the system (11) that represents meniscus profiles directly.

Type I meniscus solutions arise as codimension one intersections of W^∞ and $W^s(B)$ and therefore break under perturbations of h_B for fixed D. This agrees with previous findings [15] for a model with nonlinear curvature and small α that matching inner and outer solutions for Type I meniscus profiles fixes the film thickness achieved at $x \to \infty$. The trajectories for Type II solutions, in contrast,

are codimension zero intersections of W^∞ and $W^s(T)$. Such trajectories persist under perturbations of the parameters.

The invariant manifolds are approximated by numerically computing individual trajectories, using the LSODE ordinary differential equation solver [6], starting from appropriate initial data and then computing forwards in x for W^∞, or backwards for the stable manifolds of B and T. Specifically, for $W^s(B)$, we choose initial data $(h, v, w) = B \pm \beta\vec{u}_1$, where β is taken to be small, in the range of 10^{-8} to 10^{-3}, and $\vec{u}_1$ is the normalized eigenvector pertaining to the real negative eigenvalue of $J_F(B)$. The matrix $J_F(B)$ denotes the Jacobian of the right hand side of (11) with respect to (h, v, w), evaluated at the equilibrium B. We also remark that normalization is done here with respect to the 2-norm. For the two-dimensional manifold $W^s(T)$ we use $(h, v, w) = T + \beta\left[\cos(\theta)\vec{u}_2 + \sin(\theta)\vec{u_3}\right]$ for θ values between 0 and 2π. The vectors $\vec{u}_2$ and $\vec{u}_3$ are either the normalized eigenvectors if the two eigenvalues of $J_F(T)$ are real or, if they are complex conjugate, we use orthonormalizations of the real and imaginary parts of the eigenvectors.

For W^∞ we find approximate initial data by evaluating (15) and its first two derivatives at some sufficiently large cut-off $x = -L$; a typical choices is $L = 20$. That is, we start integrating with

$$h = -\frac{(-L)}{D} - \ln|-L| + \beta, \quad v = -\frac{1}{D} - \frac{1}{(-L)} + \beta D^{1/2}, \quad w = \frac{1}{L^2} + \beta D,$$

where $\beta = C_1 \exp(-D^{1/2}L)$ is varied within a range of values in order to trace out W^∞. For all the examples presented below, we found that using β from a range of values smaller than 0.1 was sufficient to trace out the required portion of W^∞. Increasing L typically decreased the maximum of this range of β. In terms of the alternative variables $\tilde{u} = 1/h$, $\tilde{v} = h_x$ and $\tilde{w} = h_{xx}$, increasing L and decreasing β puts the initial points closer to the equilibrium $(0, -1/D, 0)$, resulting in trajectories that approach the desired manifold more closely. Hence, it also leads to a better approximation of W^∞ in terms of the variables h, v, and w. We compared the results obtained for the original $L = 20$ to those for larger L (and smaller β) and found little difference. Specifically, the curves traced out by the intersection of the trajectories with the Poincaré-plane P defined in (16), hardly changed. This indicates that the original choice for L already yields sufficiently accurate approximations for $W^\infty \cap P$.

4.3 Results

We first investigate the phase space situation for the specific choice of $D = 0.3220$ used in Example 2 of Section 3. For a special value of $h_B = h_B^*(D) = 0.4002$, a trajectory of W^∞ connects to B, so we have a Type I solution. We note here that

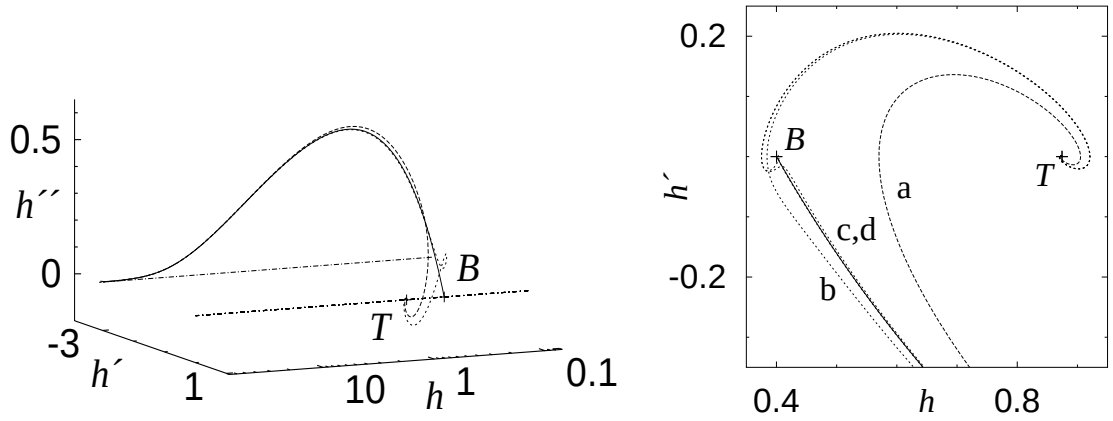

Figure 4: Two views of trajectories of W^∞ in the (h, h', h'') phase space for $D = 0.3220$ and $h_B = h_B^*(D)$. The left figure (a) is a three-dimensional view; the right figure (b) is a closer view near the stationary points, in a projection onto the h, h' plane. The solid line is a Type I trajectory that connects to B, while the dashed lines go to T and represent different Type II solutions. Dash-dotted lines in (a) denote the line $\{(h, -1/D, 0) : h > 0\}$, to which trajectories of W^∞ asymptote for $x \to -\infty$, and the positive part of the h-axis $\{(h, 0, 0) : h > 0\}$. Letters correspond to the labels in Fig. 5.

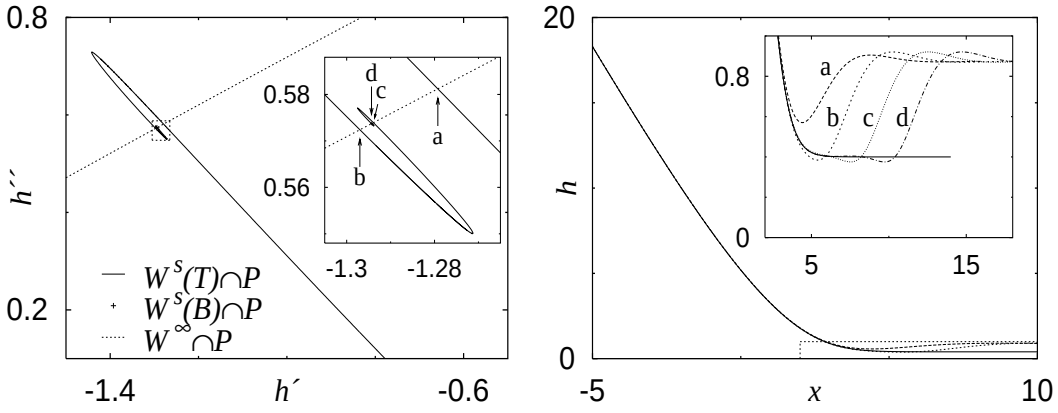

Figure 5: On the left (a) we see intersections of invariant manifolds with the Poincaré plane P defined in the text. The inset shows an enlargement of the area in the larger figure bounded by a small dashed box. The right figure (b) shows the profiles of Type I and Type II solutions. Insets show the regions in dashed boxes in more detail.

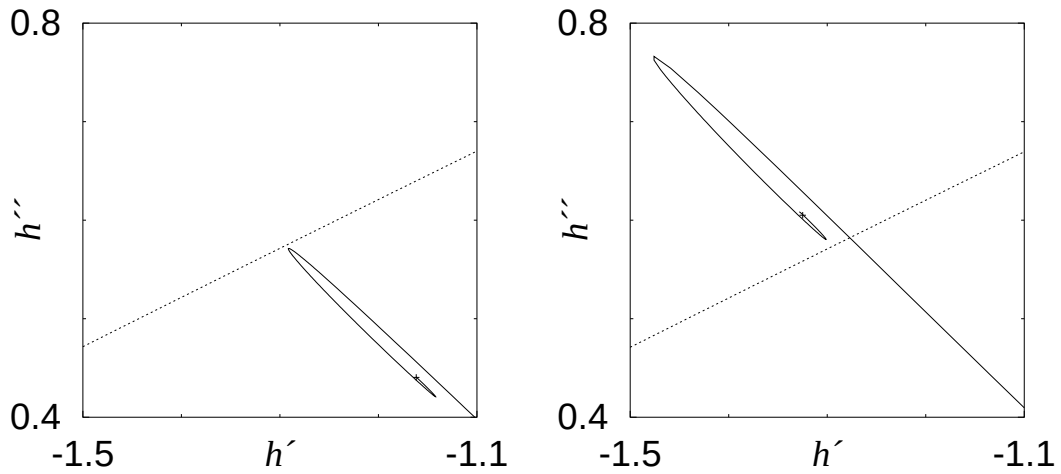

Figure 6: Poincare sections for $D = 0.3220$ and (a) (left figure) $h_B = 0.4310$ (b) (right figure) $h_B = 0.3930$. Symbols and line styles carry over from Fig. 5(a).

all numerical values appearing in this paper are given with four digits of accuracy. The Type I trajectory is shown in Fig. 4(a) by a solid line. Also shown are two dashed lines for trajectories of W^∞ that connect to T, i.e. trajectories of two different Type II meniscus solutions. In a close up of a projection of trajectories near the equilibria (Fig. 4(b)) we can identify further Type II trajectories. Shown there are the solid line for the Type I trajectory connecting to B, two distinct dashed lines labeled a and b connecting to T that are the projections of the Type II trajectories from the left figure, and two more (dashed) lines that pass very close near the equilibrium B but then connect to T, hence also represent Type II solutions. These two lines are labeled c and d and are virtually indistinguishable except in the immediate vicinity of B.

We also compute intersections of the invariant manifold with the Poincaré-plane

$$P = \{(h, v, w) : h = 2\}. \tag{16}$$

In Fig. 5(a), the point where the one-dimensional manifold $W^s(B)$, or rather, one branch of it, hits the plane is marked by a plus. Since the two other manifolds of interest here, $W^s(T)$ and W^∞, are two-dimensional, their intersections with P are curves, shown in the figure by a solid and a dashed line, respectively. The plus coincides with the dashed line indicating that W^∞ intersects $W^s(B)$, i.e. there is a Type I solution. The point where this trajectory passes through P is also the center of a spiral formed by $W^s(T) \cap P$.

The spiral arises, because trajectories from $W^s(T)$ that pass close to the equilibrium B feel the effect of the complex conjugate pair of eigenvalues and are wound into spiral around the equilibrium. This is similar to a situation described in [2, 15] for the traveling wave ODE. First note there is an orbit that connects the two equilibria, hence spirals exactly into B. Neighboring orbits approach B

but are finally expelled along one of the two branches of $W^s(B)$. Trajectories that are closer to the orbit connecting T to B spend more 'time' in the vicinity of the equilibrium and leave it, after a larger number of windings, along a curve that lies closer to $W^s(B)$. In this way the intersection of these trajectories with P traces out a spiral with an infinite number of windings centered around $W^s(B) \cap P$. Since for the special situation $h_B = h_B^*(D)$, the center of the spiral $W^s(B) \cap P$ coincides with $W^\infty \cap P$, we have an infinite number of intersections of $W^s(T) \cap P$ with $W^\infty \cap P$; each of these intersections corresponds to a different Type II meniscus solution. The first four of these intersections are shown in Fig. 5(a) and the inset, labeled by *a*-*d* according to the order in which they appear on the spiral.

Profiles of the various meniscus solutions are displayed in Fig. 5(b), with a solid line for the monotonic Type I solution, and other line styles for the four Type II solutions that correspond to the four intersections in Fig. 5(a) and are labeled accordingly. Note that in contrast to the Type I solution, the Type II solutions are non-monotonic, since they have an oscillatory structure where the meniscus passes over onto the flat film ahead of it. The solution labeled *a* has the thinnest and shallowest 'dip'. The other solutions *b*-*d* each have a minimum that is slightly below h_B within a dip that becomes wider for the higher Type II solutions.

We now change h_B, while still keeping $D = 0.3220$ fixed. For a range of values $h_B^1(D) > h_B > h_B^*(D)$ larger than $h_B^*(D)$, the center of the spiral moves to the right of $W^\infty \cap P$, but there still are multiple intersections of $W^\infty \cap P$ and $W^s(T) \cap P$. Therefore there still are multiple Type II solutions, but only a finite number of them. For h_B larger than a special value $h_B^1(D) = 0.4304$, the curves $W^s(T) \cap P$ and $W^\infty \cap P$ completely separate, so that no Type II solutions exist in this range. An example of a Poincaré-section for this case is shown in Fig. 6(a).

Similarly, for a range of values $h_B^2(D) \leq h_B < h_B^*(D)$, the center of the spiral in the Poincaré section moves to the left of $W^\infty \cap P$ but remains close enough so that we have multiple Type II trajectories, though there are again only finitely many of them. For h_B below a special value $h_B^2(D) = 0.3946$, there is only one intersection of $W^s(T) \cap P$ and $W^\infty \cap P$, as shown in Fig. 6(b), so here we have a unique Type II solution.

We obtain the same qualitative picture for a range of $0 < D < D_B$, though the special values $h_B^*(D)$, $h_B^1(D)$ and $h_B^2(D)$ change. In particular, $h_B^*(D)$ grows monotonically as D increases. The upper bound $D_B = 0.7142$ of this range is provided by where $\Delta(h_B^*(D), D)$ changes its sign, so that for larger D, all eigenvalues of the Jacobian $J_F(B)$ become real and the spiral in $W^s(T) \cap P$ disappears for $h_B = h_B^*(D)$.

Turning now to values of $D \geq D_B$, we still find a special value $h_B^*(D)$ for which Type I trajectories exist, which continues to increase monotonically with D until h_B^* reaches $2/3$. This happens for a finite value of $D = D_* = 0.8008$. We note

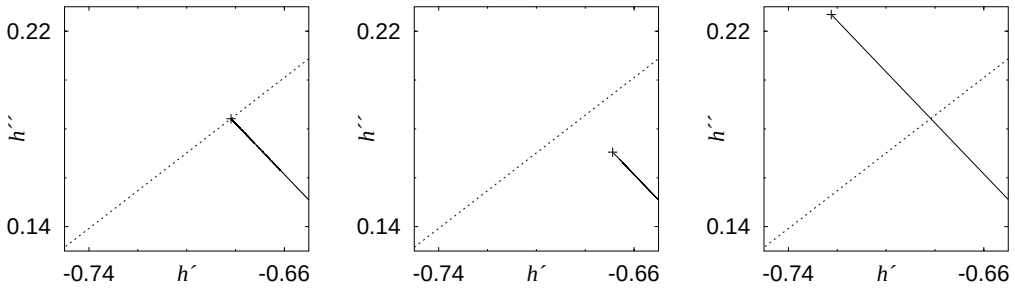

Figure 7: Poincare sections for $D = D_B = 0.7142$ and (a) $h_B = h_B^*(D) = 0.6354$ (b) $h_B = 0.6370$ (c) $h_B = 0.6300$, in order from left to right. Symbols and line styles carry over from Fig. 5(a).

that it follows from the definition of D_B that there can be at most a finite number of Type II solutions for $D \geq D_B$ and any choice of h_B.

We first limit ourselves to values of D below D_*, i.e. to the range $D_B \leq D < D_*$. The range of $D > D_*$ will be investigated further below. For $D = D_B$ and $h_B = h_B^*(D) = 0.6354$, a trajectory from W^∞ connects to the equilibrium B, so that in the corresponding Poincaré section Fig. 7(a), $W^s(B) \cap P$ coincides with $W^\infty \cap P$. There can only be a finite number of intersections of $W^\infty \cap P$ with $W^s(T) \cap P$, due to the absence of a spiral. In fact, the solid line seems to end at $W^s(B) \cap P$ without intersecting the dashed line. This leads us to conjecture that when $D_B \leq D < D_*$, there are no Type II meniscus solutions at all, for $h_B = h_B^*(D)$.

For $h_B^*(D) < h_B < 2/3$, $W^s(B) \cap P$ moves to the right of $W^\infty \cap P$. In the example shown in Fig. 7(b), we see that $W^s(T) \cap P$ ends straight at $W^s(B) \cap P$, without visibly curving around this point, so there is no possibility for an intersection of $W^s(T)$ and W^∞, i.e. there are no Type II trajectories. We conjecture that this is true for all h_B in $h_B^*(D) < h_B < 2/3$, when D satisfies $D_B \leq D < D_*$.

For $0 < h_B < h_B^*(D)$, the plus moves to the left of $W^\infty \cap P$, as seen in Fig. 7(c). Since here $\Delta(h_B; D) > 0$, the spiral in $W^s(T) \cap P$ reappears, but the rate at which it grows seems to be lower than the rate at which $W^s(B) \cap P$ and $W^\infty \cap P$ separate. In fact, in Fig. 7(c) the spiral appears to be so small that it is not visible on the scale of the figure. Hence, there is exactly one intersection of $W^s(T) \cap P$ and $W^\infty \cap P$. We conjecture that for all $0 < h_B < h_B^*(D)$ and $D_B \leq D < D_*$, we always have a unique Type II trajectory.

Finally, we consider the range of $D > D_*$. For $D = 1$ and all h_B, $0 < h_B < 2/3$, the intersection $W^s(B) \cap P$ remains at a finite distance above and to the left of $W^\infty \cap P$ in the Poincaré plane. The spiral in $W^s(T) \cap P$ is absent for a range of h_B near $2/3$, when $W^s(B) \cap P$ is closest to $W^\infty \cap P$. In other words, the Poincaré sections suggest a situation similar to the one shown in Fig. 7(c), with no Type I

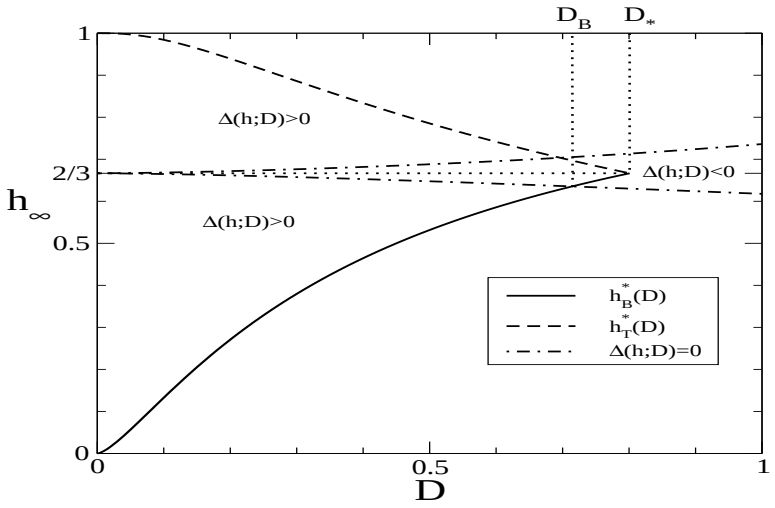

Figure 8: Occurrence of steady state solutions for different D and far-field film thicknesses h_∞. Further explanations are given in the text.

solutions, and a unique Type II solution arising from the intersection of W^∞ and $W^s(T)$. Even when a spiral is present, for moderate D and small enough h_B, we expect its center $W^s(B) \cap P$ to move away from $W^\infty \cap P$ faster than the spiral itself grows, which means that we still have just one Type II solution.

5 Summary and Outlook

Figure 8 summarizes for which values of D and h_∞ we find a stationary meniscus solution with $h \to h_\infty$ for $x \to \infty$. All solutions that have a far-field thickness below $h_\infty = 2/3$ (dotted horizontal line in the figure) are Type I solutions, the ones with larger thickness are of Type II.

For $D < D_*$, there is a single branch of Type I solutions, for which $h_\infty = h_B^*(D) \to 2/3$ as $D \to D_*$ from below. For $D \to 0$, the numerical data shows that the film thickness for this branch of solutions tends to zero; in fact, closer inspection in a log-log plot indicates that $h_\infty = h_B^*(D) \sim D^{3/2}$. Note however, that the approximations used in the derivation of (6) are only valid if $D \gg \epsilon$. Indeed, previous results by Münch [15] for near vertical positions on stationary meniscus solutions for (1) show that in the limit $\epsilon, D \to 0$, $D \ll \epsilon$, the film thickness behaves like $\epsilon^{3/2}$, i.e. decays more slowly than the result $\sim D^{3/2}$ obtained from the lubrication model (6).

Type II solutions exist in the $0 < D < D_B$ for thicknesses $h_\infty \geq h_T^1(D)$, with multiple solutions arising in a thin strip $h_T^1(D) < h_\infty \leq h_T^2(D)$ that contains $h_T^*(D)$. Here $h_T^1(D)$ is defined as the root $h > 2/3$ of $f(h) = f(h_B^1(D))$, where

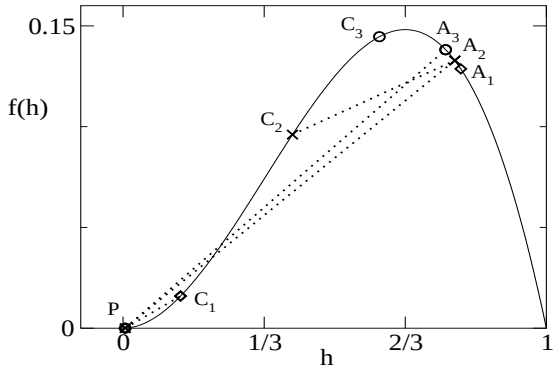

Figure 9: Situation on the graph of the flux function $f(h) = h^2 - h^3$ for each of the three examples of numerical simulations introduced in Section 3. Boxes, crosses and circles mark the points $(b, f(b))$ (label P), $(h_{\rm uc}, f(h_{\rm uc}))$ (labels A_i) and $(h_B^*, f(h_B^*))$ (labels C_i), with a different symbol for each example $i = 1, 2$ and 3. Dotted lines indicate chords for the shock wave profiles that appear in the simulations.

$h_B^1(D)$ is the special value introduced in the previous section; the values $h_T^*(D)$ and $h_T^2(D)$ are defined analogously. For $D_B < D < D_*$, we have the simpler situation of either no Type II solutions if $h_\infty \leq h_T^*(D)$, or exactly one, if $h_\infty > h_T^*(D)$. This implies that $h_T^1(D)$ and $h_T^2(D)$ tend to $h_T^*(D)$ as D approaches D_B from below.

A complementary diagram to Fig. 8 that maps out which wave structures arise at the contact line for different values of the parameter D and left states h_∞ (and selected precursor thicknesses b) is given in [13]. Overlapping the two diagrams yields additional information about which dynamics are possible for a thin film emerging from the meniscus, and which type of meniscus solution is established in the long run, for different values of D. An outline of the picture that emerges is given here by discussing the three examples introduced in Section 3; a fuller account that also investigates the stability of the meniscus solutions will be given in an upcoming paper.

For Example 1, the thickness $h_B^*(D)$ of the Type I solution for $D = 0.1021$ is fairly small; it corresponds to label C_1 on the graph of the flux function (Fig. 9). Theory [2, 13] predicts that for a class of monotonic initial data connecting b with a left state below a certain threshold, a single compressive wave arises. This threshold depends on b and D, and can be determined by investigating the phase space for the traveling wave ODE of the lubrication model (6). For the choice of b and D in this example, $h_B^*(D)$ indeed lies below the threshold. So we observe the formation of a single compressive wave and a Type I meniscus solution. The left state of the wave is determined by the unique far-field thickness of the Type I meniscus, i.e. $h_\infty = h_B^*(D)$, which does not depend on b. The speed

of the compressive wave is given by the slope of the chord connecting C_1 and B in Fig. 9.

Raising the value of D to 0.3220 in Example 2 significantly increases $h_B^*(D)$ so that it is now larger than the threshold, which has hardly changed. The authors of [2, 13] predict for this case the formation of a double compressive/undercompressive wave, with a unique b- and D-dependent left state $h_{\rm uc}$ for the leading undercompressive wave. Its value can again be obtained from the traveling wave ODE. The chords A_2C_2 and A_2P for the two waves have positive slope, indicating that both waves move away from the meniscus, albeit with different speeds. The meniscus converges to a Type I solution which determines $h_\infty = h_B^*(D)$, as in the previous example.

Example 3 uses an even larger value of D, so that now, $h_B^*(D)$ is not only above the slightly increased threshold but is in fact larger than $h_{\rm uc}(D, b)$. Therefore, the chord A_3C_3 for the trailing Lax wave would have a negative slope, and so the Lax wave would move backwards! Therefore, no Lax wave is able to separate from the meniscus. However, an undercompressive wave still appears, and this has a positive speed. The meniscus settles into a Type II solution with a far-field that is determined by the undercompressive height $h_{\rm uc}(D, b) > 2/3$.

Acknowledgments

AM was supported by a Heisenberg scholarship (DFG grant MU 1626/3-1) and by the DFG Research Center FZT 86, "Mathematics for key technologies". AM thanks Michael Shearer, Tom Witelski, Klaus Schneider, Matthias Wolfrum and Barbara Wagner for helpful discussions. PE is currently supported through Project C10 of the DFG Research Center FZT 86.

References

[1] A. L. Bertozzi, A. Münch, X. Fanton, and A. M. Cazabat. Contact line stability and 'undercompressive shocks' in driven thin film flow. *Phys. Rev. Lett.*, 81(23):5169–5172, December 1998.

[2] A. L. Bertozzi, A. Münch, and M. Shearer. Undercompressive waves in driven thin film flow. *Physica D*, 134:431–464, 1999.

[3] P. Carles and A.-M. Cazabat. The thickness of surface-tension-gradient-driven spreading films. *Journal of Colloid and Interface Science*, 157:196–201, 1993.

[4] A. M. Cazabat, F. Heslot, S. M. Troian, and P. Carles. Finger instability of thin spreading films driven by temperature gradients. *Nature*, 346(6287):824–826, August 1990.

[5] X. Fanton, A. M. Cazabat, and D. Quéré. Thickness and shape of films driven by a Marangoni flow. *Langmuir*, 12(24):5875–5880, 1996.

[6] A. C. Hindmarsh. ODEPACK, a systematized collection of ODE solvers. In R. S. Stepleman et al., editors, *Scientific Computing*, volume 1 of *IMACS Transactions on Scientific Computation*, pages 55–64. North-Holland, Amsterdam, 1983.

[7] L. M. Hocking. Meniscus draw-up and draining. *European Journal of Applied Mathematics*, 12:195–208, 2001.

[8] D. E. Kataoka and S. M. Troian. A theoretical study of instabilities at the advancing front of thermally driven coating films. *Journal of Colloid and Interface Science*, 192:350–362, 1997.

[9] D. E. Kataoka and S. M. Troian. Stabilizing the advancing front of thermally driven climbing films. *Journal of Colloid and Interface Science*, 203:335–344, 1998.

[10] H. S. Kheshgi, S. F. Kistler, and L. E. Scriven. Rising and falling film flows: Viewed from a first-order approximation. *Chemical Engineering Science*, 47:683–694, 1992.

[11] L. Landau and B. Levich. Dragging of a liquid by a moving plate. *Acta Physicochim. URSS*, 17:42–54, 1942.

[12] V. Ludviksson and E. N. Lightfoot. The dynamics of thin liquid films in the presence of surface-tension gradients. *Am. Inst. Chem. Engrs. J.*, 17(5):1166–1173, 1971.

[13] A. Münch. Shock transitions in Marangoni-gravity driven thin film flow. *Nonlinearity*, 13:731–746, 2000.

[14] A. Münch. The role of the meniscus in the formation of non-classical shocks in thin marangoni-gravity driven films, Nov. 2001. Habilitation thesis, Technical University of Munich.

[15] A. Münch. The thickness of a Marangoni-driven thin liquid film emerging from a meniscus. *SIAM J. Appl. Math*, 62(6):2045–2063, 2002.

[16] A. Münch. Pinch-off transition in Marangoni-driven thin films. *Physical Review Letters*, 91(1):id: 016105, 2003.

[17] A. Münch and A. L. Bertozzi. Rarefaction-undercompressive fronts in driven films. *Physics of Fluids*, 11(1):2812–2814, Oct. 1999.

[18] A. Münch and B. A. Wagner. Numerical and asymptotic results on the linear stability of a thin film spreading down a slope of small inclination. *European Journal of Applied Mathematics*, 10:297–318, 1999.

[19] M. Schneemilch and A. M. Cazabat. Shock separation in wetting films driven by thermal gradients. *Langmuir*, 16:9850–9856, 2000.

[20] M. Schneemilch and A. M. Cazabat. Wetting films in thermal gradients. *Langmuir*, 16:8796–8801, 2000.

[21] L. W. Schwartz. On the asymptotic analysis of surface-stress-driven thin-layer flow. *Journal of Engineering Mathematics*, 39:171–188, 2001.

[22] S. D. R. Wilson. The drag-out problem in film coating theory. *Journal of Engineering in Mathematics*, 16(3):209–221, 1982.